Magnetic surface domain imaging of uncapped epitaxial FeRh(001) thin films across the temperature-induced metamagnetic transition

Cite as: AIP Advances **6**, 015211 (2016); https://doi.org/10.1063/1.4940758
Submitted: 02 September 2015 • Accepted: 11 January 2016 • Published Online: 22 January 2016

Xianzhong Zhou, Frank Matthes, Daniel E. Bürgler, et al.

Magnetic surface domain imaging of uncapped epitaxial FeRh(001) thin films across the temperature-induced metamagnetic transition

Xianzhong Zhou,[a] Frank Matthes, Daniel E. Bürgler,[b]
and Claus M. Schneider
Peter Grünberg Institut, Electronic Properties (PGI-6) and Jülich-Aachen Research Alliance, Fundamentals of Future Information Technology (JARA-FIT), Forschungszentrum Jülich, D-52425 Jülich, Germany

(Received 2 September 2015; accepted 11 January 2016; published online 22 January 2016)

The surface magnetic domain structure of *uncapped* epitaxial FeRh/MgO(001) thin films was imaged by *in-situ* scanning electron microscopy with polarization analysis (SEMPA) at various temperatures between 122 and 450 K. This temperature range covers the temperature-driven antiferromagnetic-to-ferromagnetic phase transition in the body of the films that was observed *in-situ* by means of the more depth-sensitive magneto-optical Kerr effect. The SEMPA images confirm that the interfacial ferromagnetism coexisting with the antiferromagnetic phase inside the film is an intrinsic property of the FeRh(001) surface. Furthermore, the SEMPA data display a reduction of the in-plane magnetization occuring well above the phase transition temperature which, thus, is not related to the volume expansion at the phase transition. This observation is interpreted as a spin reorientation of the surface magnetization for which we propose a possible mechanism based on temperature-dependent tetragonal distortion due to different thermal expansion coefficients of MgO and FeRh. [http://dx.doi.org/10.1063/1.4940758]

I. INTRODUCTION

The CsCl-ordered, equiatomic alloy of Fe and Rh is a magnetic material with a unique temperature-induced metamagnetic transition from antiferromagnetic (AFM) *below* the transition temperature $T_{trans} \approx 350$ K[1] to ferromagnetic (FM) *above* T_{trans}. Exchange systems comprising an FeRh layer showing a temperature-induced metamagnetic transition and a hard magnetic layer are intensively discussed as a promising approach for heat-assisted magnetic recording.[2,3] An AFM memory resistor operating at room temperature has recently been demonstrated by combining the temperature-induced metamagnetic transition of FeRh thin films with the AFM analogue of the anisotropic magnetoresistance effect.[4] Furthermore, the metamagnetic transition of FeRh is accompanied by an increase of the volume of the unit cell by about 1%[1] reflecting a significant coupling between magnetic and structural properties. On the basis of this coupling, electrical control of magnetism above room temperature (RT) has been demonstrated in multiferroic heterostructures of FeRh in combination with a ferroelectric/piezoelectric material.[5]

Although the temperature-induced metamagnetic transition from AFM to FM in bulk FeRh has already been found decades ago,[1,6–8] the mechanism of the transition is still under debate, especially concerning the surface magnetic properties of single-crystalline FeRh thin films,[9–13] which can be different from the bulk, but are of utmost importance for potential applications. Up to now,

[a]Present address: School of Physics and Engineering and State Key Laboratory of Optoelectronic Materials and Technologies, Sun Yat-sen University, 510275 Guangzhou, China
[b]Corresponding author: d.buergler@fz-juelich.de

all reports in literature on the surface magnetic properties of FeRh thin films deal with capped films (*e.g.* capped with Pt,[9] Au,[14] MgO,[14,15] or Al[13]) or with oxidized surfaces.[13] Capping layers typically introduce strain and, thus, affect the magnetic properties *via* magneto-elastic coupling. In addition, capping materials can diffuse into FeRh or chemically react with the alloy. Hence, the surface magnetic properties of FeRh are inevitably changed by capping layers.[16,17] This also holds for contaminated and oxidized surfaces.

As expected for a first-order phase transition, the AFM and FM phases of FeRh coexist across the transition.[9,14,15,18,19] Baldasseroni *et al.*[13] recently imaged FM domains in 90 nm thick single-crystalline FeRh films on MgO(001) by x-ray magnetic circular dichroism (XMCD) and photoemission electron microscopy (PEEM). The coexistence of laterally separated FM and AFM phases as well as temperature-induced nucleation and growth of FM domains across the transition were directly imaged on oxidized FeRh films. In contrast, films capped with 2.5 nm Al showed stable FM domains at the FeRh/Al interface below the metamagnetic transition temperature of the film. Interfacial ferromagnetism of this form was also observed in XMCD measurements by Ding *et al.*[14] for FeRh thin films capped with MgO or Au. The occurrence of stable interfacial FM domains below the bulk transition temperature is assumed to be related to interdiffusion, deviations in composition (*e.g.* Fe deficiency), or strain effects induced by the capping layers.[13,14]

Here, we use *in-situ* scanning electron microscopy with polarization analysis (SEMPA) to directly image the intrinsic magnetic domain structure at the surface of *uncapped* 10 nm thick single-crystalline FeRh(001) films at various temperatures from far below to well above the metamagnetic phase transition.

II. EXPERIMENTAL SETUP AND PROCEDURES

All steps of the experiment, substrate cleaning, thin film deposition and characterization, as well as SEMPA imaging were performed in a multi-chamber ultra-high vacuum (UHV) system without breaking the vacuum.

The UHV system comprises among other equipment an e-beam evaporator with five pockets for thin film growth, Auger electron spectroscopy (AES) and low-energy electron diffraction (LEED) for chemical and structural surface characterization, an *in-situ* magneto-optical Kerr effect (MOKE) setup, and an UHV-compatible scanning electron microscope with polarization analysis (SEMPA). For the MOKE measurements we used a modulated laser with a wave length of 670 nm incident at 45° and a Glan-Taylor prism to linearly polarize the incoming beam. The reflected light is split in a Wollaston prism into two orthogonally polarized beams. Their intensities are measured by photodiodes and lock-in detection. The intensity difference normalized by the sum is proportional to the Kerr angle, which for the here used longitudinal geometry is approximately proportional to the in-plane magnetization component along the field axis, *i.e.* the quantity to be measured. The information depth of the MOKE is given by the penetration depth of photons in the visible range into metals, which exceeds 20 nm.[20] Hence, the MOKE probes the surface as well as the body of our 10 nm thick films. In contrast, SEMPA[21–24] is extremely surface-sensitive and yields information about the magnetic microstructure at the very surface.[25,26] The SEMPA setup consists a Zeiss Gemini electron column with a thermal field emission cathode and a SPLEED detector from FOCUS.[27] For magnetic domain imaging we operated the column at a primary energy of 5 keV and a beam current of 1 nA, and the working distance was 11 mm. The spin polarization of the secondary electrons (SE) with kinetic energies below about 10 eV is analyzed employing the spin-dependent scattering of low-energy electrons from a W(001) crystal. The scattering geometry is that of a reverse-view LEED setup (SPLEED stands for spin-polarized low-energy electron diffraction).[28,29] The mean scattering potential is 104.5 eV such that the four structurally equivalent (2,0) beams hit the four symmetrically aligned multi-channel plate (MCP) detectors. The angle between the optical axes of the SEM column and the SPLEED detector is 64°. We adjusted the normal of the sample surface collinear to the optical axis of the SPLEED detector to be sensitive to the two in-plane components $M_{x,y}$ of the surface magnetization, which are

to a good approximation proportional to the spin polarization (P_x, P_y) of the emitted SE

$$M_x \propto P_x = \frac{1}{S} A_x \quad \text{with} \quad A_x = \frac{N_{(2,0)} - N_{(\bar{2},0)}}{N_{(2,0)} + N_{(\bar{2},0)}} \tag{1}$$

$$M_y \propto P_y = \frac{1}{S} A_y \quad \text{with} \quad A_y = \frac{N_{(0,2)} - N_{(0,\bar{2})}}{N_{(0,2)} + N_{(0,\bar{2})}}. \tag{2}$$

$N_{(i,j)}$ are the intensities of the diffraction spots $(i,j) \in \{(2,0),(\bar{2},0),(0,2),(0,\bar{2})\}$ measured by the four MCPs. S is the Sherman function (spin-resolving efficiency of the detector), which relates the spin asymmetries (A_x, A_y) to the spin polarization of the SE. The Sherman function has previously been measured for the employed type of SPLEED detector using a GaAs-based electron source with well-defined spin polarization. For the scattering at 104.5 eV into the (2,0) beams S equals -0.27.[27,29] In practice, S of a SEMPA setup depends on the operation conditions of the SPLEED detector and on the energy distribution of the SE emitted from the sample material.[30] Therefore, we present in the following the measured spin asymmetries (A_x, A_y).

The W(001) crystal of the SPLEED detector was prepared following the procedures provided by FOCUS:[31] Typically 15 cycles of flashing to 1350 K for 10 s and waiting for 50 s in 5×10^{-8} mbar O_2 partial pressure to deplete carbon bulk contamination in the interface region (hot oxygen treatment) and subsequent flashing at 2300 K for 10 s to remove tungsten oxides from the surface (oxide-flash) are applied after venting the system. Although the chamber housing the SEMPA is separated from the preparation chamber by a gate valve allowing to permanently keep the pressure in the low 10^{-11} mbar range, residual gas (mainly hydrogen and CO) accumulates on the W(001) surface and reduces the Sherman function by several percent per hour of operation.[27] Regular cycles of annealing at 1500 K for 10 s applied before each measurement to remove CO contamination (CO-flash) maintained the optimized operation conditions of the crystal. The sample stage in the SEMPA chamber is equipped with a LHe flow cryostat, a resistive heater, and a thermocouple, which allow controlling the sample temperature in the range between 30 and 500 K. The precise positioning of the sample with respect to the electron column and the SPLEED detector is achieved with three integrated piezo motors for linear x–, y–, and z–motion and one rotational degree of freedom about the main manipulator axis. The SEMPA chamber is shielded with μ-metal to minimize detrimental magnetic stray fields.[27]

III. SAMPLE PREPARATION

Commercially available MgO(001) substrates were cleaned with isopropanol in an ultrasonic bath, clamped onto a Mo sample holder, and transferred into the UHV system. The *in-situ* treatment consisted of degassing at 500 K for several hours until the pressure in the preparation chamber reached 1×10^{-10} mbar followed by annealing at 900 K for one hour in 1×10^{-7} mbar O_2 partial pressure to remove C contamination.[32] After switching off the O_2 supply, the sample was slowly cooled to RT and exhibited a clear quadratic (1×1) LEED pattern [Fig. 1(a)].

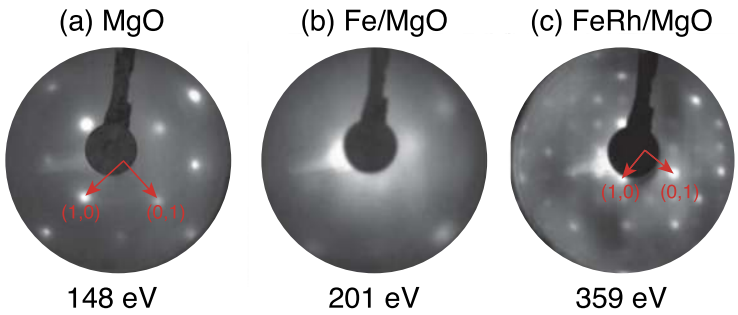

FIG. 1. LEED patterns taken at RT of (a) clean MgO(001) at 148 eV, (b) Fe(001)/MgO(001) at 201 eV, and (c) FeRh(001)/MgO(001) after annealing at 359 eV.

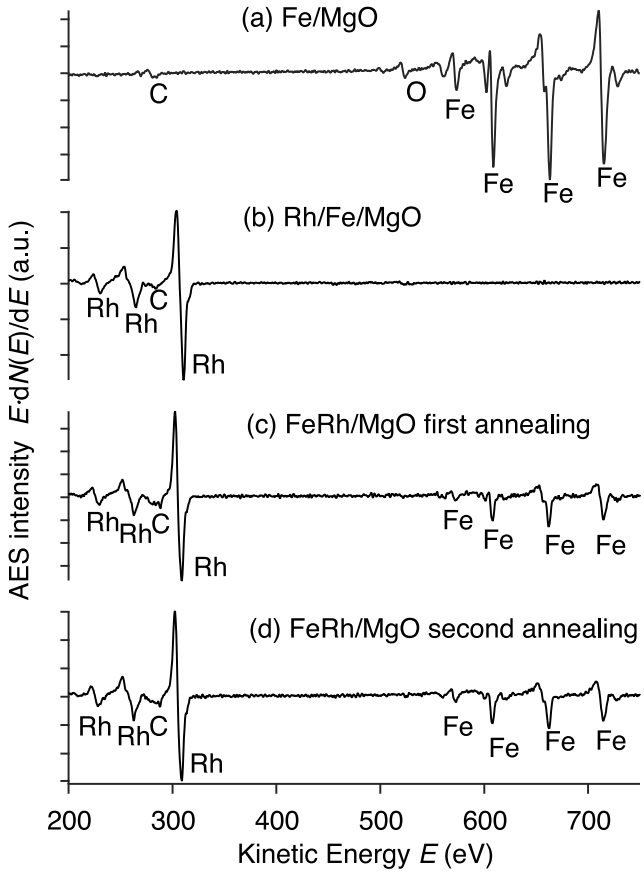

FIG. 2. AES spectra of (a) Fe/MgO(001), (b) Rh/Fe/MgO(001) before annealing, (c) FeRh/MgO(001) after the first annealing cycle (2 hours at 900 K), and (d) FeRh/MgO(001) after the second annealing cycle.

The vapor pressures of Fe and Rh differ in the temperature range between RT and the melting temperature of Fe by several orders of magnitude[33] prohibiting stoichiometric deposition of equiatomic FeRh by thermal evaporation of an FeRh alloy. Therefore, we successively evaporate Fe and Rh from different pockets of the e-beam evaporator followed by an extended high-temperature annealing step to activate interdiffusion and the formation of the equiatomic FeRh alloy. Lommel,[34] who described this deposition route already in 1966, showed that it works for Fe and Rh sublayer thicknesses up to 80 nm. Aiming at a final FeRh alloy thickness of only 10 nm, we first deposited $d_{\mathrm{Fe}} = 5$ nm Fe at a rate of 0.02–0.03 Å/s with the substrate held at RT. The AES spectrum of the Fe film in Fig. 2(a) shows dominant Fe peaks and traces of oxygen and carbon most likely originating from the residual gas. The quadratic (1×1) LEED pattern [Fig. 1(b)] of the Fe surface indicates epitaxial growth. The rather diffuse spots are attributed to increased surface roughness and defect density caused by the Fe growth at RT,[35] which, however, in this stage of the alloy preparation are no matter of concern.

In a next step we evaporated again at a rate of 0.02–0.03 Å/s with the substrate held at RT $d_{\mathrm{Rh}} = \frac{\rho_{\mathrm{Fe}}}{\rho_{\mathrm{Rh}}} \frac{m_{\mathrm{Rh}}}{m_{\mathrm{Fe}}} d_{\mathrm{Fe}} \approx 5.8$ nm Rh, where $\rho_{\mathrm{Fe,Rh}}$ and $m_{\mathrm{Fe,Rh}}$ are the density and the atomic mass of Fe and Rh, respectively. This thickness ratio results in an equal number of Fe and Rh atoms per unit area required for the formation of the equiatomic FeRh alloy. The AES spectrum taken immediately after Rh deposition [Fig. 2(b)] shows that Fe does not diffuse to the surface and only weak carbon contamination. LEED spots could not be observed in this stage, indicating a highly disordered surface. In order to heal the surface structure and activate the interdiffusion of Fe and Rh to induce the formation of an ordered FeRh alloy film, the sample was annealed for two hours at 900 K. This annealing procedure was applied two times to check whether the film composition and structure

have reached a stable state. The AES spectra taken after the first and the second annealing cycle in Figs. 2(c) and 2(d) do not show significant differences. The Fe:Rh ratios determined from the spectra taking into account the corresponding sensitivity factors[36] were 49.8% : 50.2% after the first and 49.5% : 50.5% after the second annealing cycle, respectively. These values agree within the estimated error of 1% with the nominal equiatomic composition. Thus, we conclude that one annealing cycle at 900 K for two hours is sufficient to form the FeRh alloy and that this alloy is stable against further heating. The LEED pattern in Fig. 1(c) was taken after the second annealing cycle but is also representative for the surface after the first cycle and reveals that the FeRh alloy film is epitaxially grown and exhibits a well-ordered (001) surface.

IV. SURFACE DOMAIN IMAGING

In-situ MOKE measurements were performed immediately after the sample preparation to investigate the magnetic properties of the body of the films and to verify the presence of the metamagnetic transition. Kerr angle *versus* external field measurements taken at RT and 143 K are shown in Fig. 3. Clear magnetic hysteresis with an loop opening of 45.5 mT is observed at RT and indicates FM ordering. In contrast, there is no opening of the curve at 143 K meaning that the film has undergone the phase transition to AFM with a transition temperature T_{trans} below RT, which is lower than the range of transition temperatures reported in literature for FeRh bulk specimens (310 – 350 K)[7,37–39] and sputtered FeRh thin films (320 – 400 K).[9,13,40] As indicated by Maat *et al.*,[9] strain strongly decreases the transition temperature of single-crystalline films. We assume that in our case the deposition route, the MgO(001) substrate, and the relatively low thickness of only 10 nm result in epitaxial FeRh thin films with larger strain compared to sputtered FeRh thin films and bulk FeRh samples.

The evolution of the remanent *surface* domain structure upon cooling and heating across the phase transition in the body of the film was imaged by SEMPA and is shown in Fig. 4. For each pixel (x, y) of the SEMPA images the local in-plane spin asymmetry vector $\mathbf{A}(x, y) = (A_{\mathrm{x}}, A_{\mathrm{y}})$ is calculated from the four measured intensities $N_{(\mathrm{i,j})}$ according to Eqs. (1) and (2). The resulting vector field is presented in a false-color representation according to the color-wheel in Fig. 4(i). The color indicates the direction of $\mathbf{A}(x, y)$ and the color saturation the spin asymmetry magnitude $|\mathbf{A}(x, y)| = \sqrt{A_{\mathrm{x}}^2 + A_{\mathrm{y}}^2}$ in the range between 0 (white in the center of the color-wheel) and 7% (saturated colors at the circumference of the color-wheel). The measurement cycle for the data in Fig. 4 was (a) first cooled to 122 K, (b) then directly heated to 450 K, (c-e) subsequently cooled in steps of

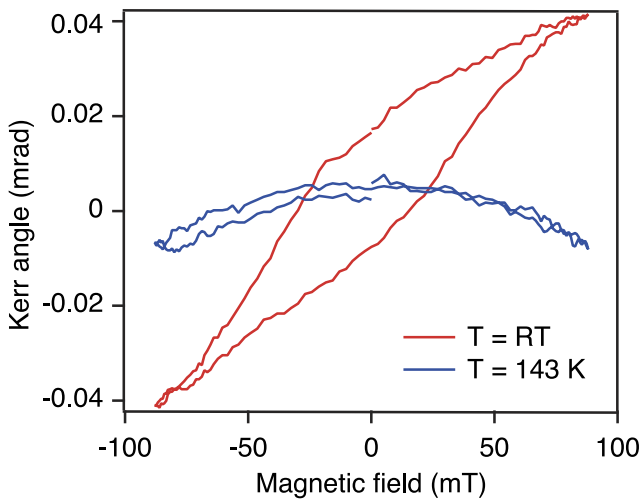

FIG. 3. Longitudinal MOKE hysteresis loops of a 10 nm thick equiatomic FeRh film on MgO(001) measured with the external field applied along a MgO[110] direction taken at RT (red) and 143 K (blue), respectively.

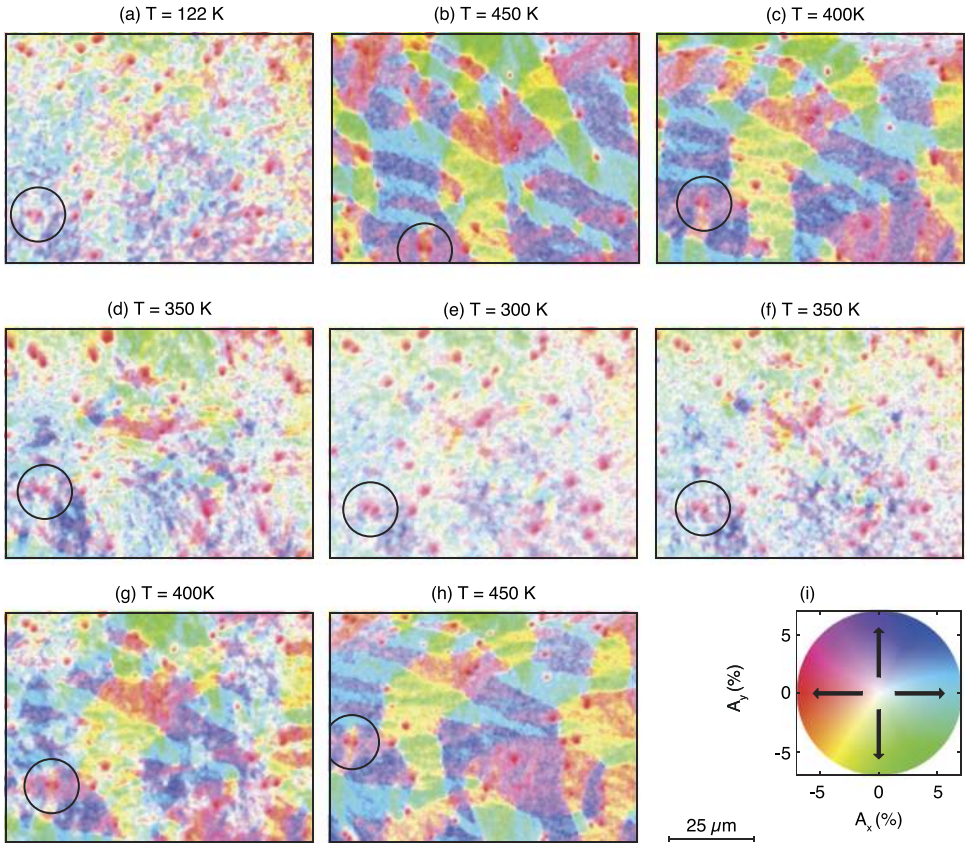

FIG. 4. (a-h) SEMPA domain images of an uncapped 10 nm thick FeRh(001) film on MgO(001) measured in zero field and at different temperatures as indicated. Images are taken in the sequence (a) to (h) and show the same sample area: Black circles mark the same features. (i) Color-wheel for the representation of the in-plane spin asymmetry vectors $\mathbf{A}(x, y) = (A_x, A_y)$ and scale bar for all images.

50 K to 300 K, and (f-h) finally heated again in steps of 50 K to 450 K. A CO-flash to 1500 K was applied to the W(001) crystal of the SPLEED detector prior to each SEMPA measurement to reduce the effect of its contamination on the Sherman function.

Ferromagnetic domains represented by the spin asymmetry vectors $\mathbf{A}(x, y)$ covering the whole surface are imaged at all temperatures, *i.e.* below and above the phase transition temperature observed for the body of the same film by *in-situ* MOKE (Fig. 3) as well as those reported in literature.[7,9,13,37–40] Thus, we observe for uncapped FeRh thin films stable interfacial ferromagnetism down to at least 122 K. Large domains with straight domain walls and strong in-plane magnetization exist at 450 and 400 K [Figs. 4(b),4(c),4(g), and 4(h)], whereas smaller and irregularly shaped domains prevail at 350 K and below [Figs. 4(d),4(d), and 4(f)] down to the lowest temperature of 122 K [Figs. 4(a)] well below the transition temperature of the body of the film, which according to the MOKE data in Fig. 3 lies between RT and 143 K. Upon heating the domains grow again between 300 to 450 K and form a similar but not identical domain structure as before [compare Figs. 4(b) and 4(h)]. There is a weak temperature hysteresis at 400 K. Upon cooling large domains prevail at 400 K [Fig. 4(c)], whereas upon heating there are still some small domains visible at this temperature [Fig. 4(g)] that only disappear after reaching 450 K [Fig. 4(h)]. The drastic change in domain size and structure between 350 to 400 K implies temperature-induced domain motion, nucleation, and formation at the surface of *in-situ* prepared, uncapped FeRh films. Temperature-driven nucleation and formation of surface magnetic domains in FeRh thin films with thin capping layers has previously been reported by Baldasseroni *et al.*,[13] who related the change in the domain morphology to the metamagnetic transition. In our case, however, the surface domain structure changes above RT, whereas the phase transition in the body of the film is below RT.

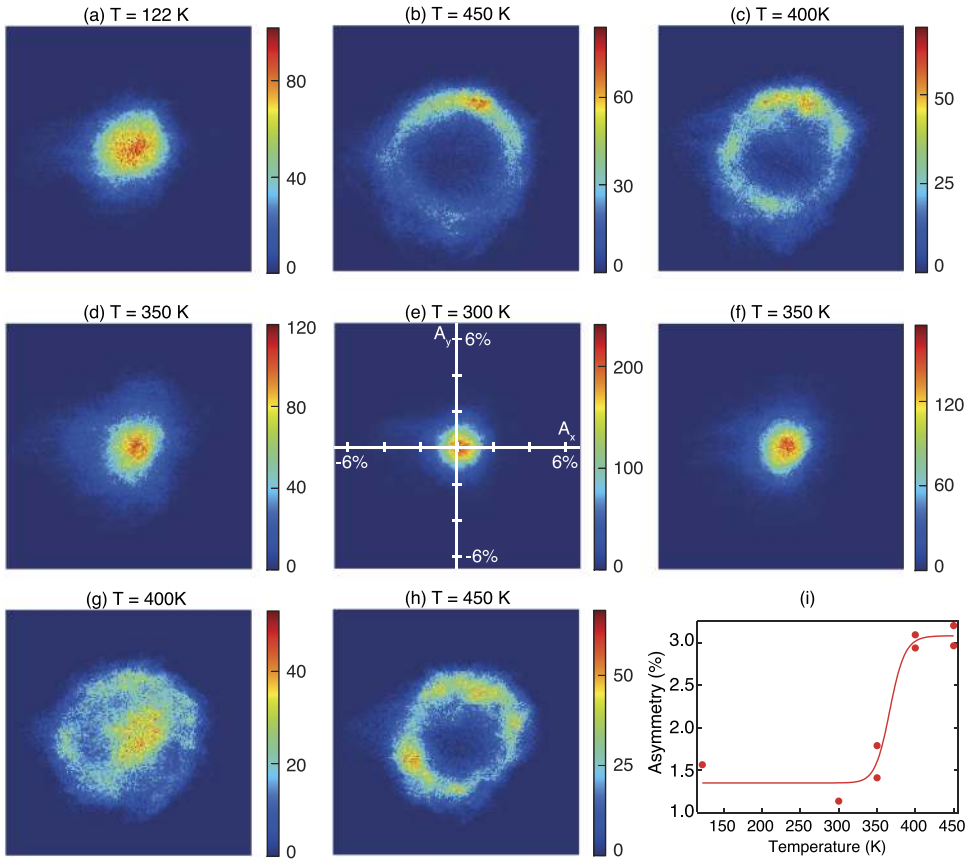

FIG. 5. (a-h) Two-dimensional spin asymmetry histograms of the temperature-dependent SEMPA images in Figs. 4(a)-4(h) showing the probability densities of the spin asymmetry vectors. (i) Temperature-dependent spin asymmetry determined from the radial extent of the distributions in (a-h). The solid line is as guide to the eyes.

In order to gain deeper insight into the temperature-induced changes of the surface domain structure in Fig. 4, two-dimensional spin asymmetry histograms of the SEMPA images are calculated and displayed in Fig. 5. Each histogram is obtained by plotting the local spin asymmetry vectors $\mathbf{A}(x, y) = (A_x, A_y)$ from the origin in the (A_x, A_y)-plane [see coordinate system in Fig. 5(e)]. The color code represents the frequency of a certain spin asymmetry vector. Obviously, the distributions of the spin asymmetry and hence in-plane magnetization direction are rather uniform at all temperatures, indicating that there is no significant in-plane anisotropy in the FeRh(001) film. This is in contrast to the Al-capped FeRh films studied by Baldasseroni *et al.*[13] that exhibited two pairs of equivalent FeRh [100] in-plane directions as preferred orientation of FM domains (easy axes). A weak preference of spin asymmetry vectors along the [110]-axis in our case, best seen in Fig. 5(h), is a consequence of the remanent state after applying a magnetic field along the [110]-axis during the preceding MOKE measurements (Fig. 3). The spin asymmetry magnitudes $|\mathbf{A}(x, y)|$, however, show a strong dependence on temperature as seen from the clearly different radii of the histogram distributions as plotted in Fig. 5(i). There is a step-like and reversible change from about 1.5% to 3.0% between 350 and 400 K. This behavior is not related to the first-order transition from AFM to AF in the body of the films, which in our films occurs below RT. The reversibility of the domain images in Fig. 4 and the radius of spin asymmetry distribution in Fig. 5(i) indicates that the surface magnetism of the FeRh film is not modified by thermally induced irreversible changes to the film neither by surface contamination during the entire SEMPA measurement time.

Previously, Cao *et al.*[10] and Bordel *et al.*[12] have observed a spin reorientation transition in 150 nm thick, sputtered, and single-crystalline FeRh films on MgO. In both reports the spin reorientation transition occurs at the metamagnetic transition temperature and was explained by an sign

change of the magneto-elastic anisotropy energy due to the abrupt volume expansion at the AFM-to-FM phase transition[10] or by the dependence of the strain-induced magneto-crystalline anisotropy energy (MCA) on the magnetic phase, *i.e.* FM or AFM phase.[12] In particular, density-functional theory (DFT) calculations of Bordel *et al.*[12] reveal that the MCA of FeRh strongly depends on the tetragonal distortion ratio c/a and changes sign when the magnetic order switches from FM to AFM: $c/a < 1$ favors in-plane or out-of-plane magnetization in the FM and AFM phase, respectively, and *vice versa* for $c/a > 1$. For $c/a = 1$ the strain-induced MCA vanishes for both magnetic phases. The spin reorientation for FeRh/MgO from in-plane in the AFM phase to out-of-plane in the FM phase in Ref. 12 is thus explained by the substrate-induced tetragonal distortion ($c/a > 1$) and the sign change of the MCA at the metamagnetic transition.

Based on these findings we propose a mechanism for the observed step-like and reversible change of the spin asymmetry distributions. We assume that it results from a reorientation of the magnetic moment at the very surface from in-plane above 400 K to tilted towards the surface normal below 350 K, which leads to a reduction of the in-plane spin asymmetry $\mathbf{A}(x, y)$ measured by SEMPA and displayed in Fig. 5. Note that the images in Figs. 4(g) and 5(g) depict a state, where in-plane magnetized and tilted areas coexist. Interestingly, the transition from large domains above 400 K to smaller ones at low temperature coincides with the proposed spin reorientation transition. This observation can naturally be explained by the demagnetizing field of the out-of-plane component of the magnetization that favors the formation of smaller domains with opposite out-of-plane magnetization components. In contrast to Bordel *et al.*,[12] the surface is in our case FM in the whole temperature range. Nevertheless, the results of the DFT calculations in Ref. 12 predict a spin reorientation from in-plane (negative MCA) to out-of-plane (positive MCA), if c/a increases from $c/a < 1$ above 400 K to $c/a > 1$ below 350 K. A possible explanation for such a temperature dependence of the distortion in our films can be given on the basis of the quite different linear thermal expansion coefficients α of MgO and FeRh: $\alpha_{\mathrm{MgO}} \geq 10 \times 10^{-6}\,\mathrm{K}^{-1}$ (above RT)[41,42] is almost twice as large as $\alpha_{\mathrm{FeRh}} = 6 \times 10^{-6}\,\mathrm{K}^{-1}$ in the FM phase.[43] The epitaxy between the FeRh(001) film and the MgO(001) substrate locks the in-plane lattice parameters of the FeRh thin film a and b ($a = b$) to that of the MgO surface. Upon cooling the MgO substrate and hence a and b shrink stronger than required by bulk FeRh. The too strong decrease of a and b is compensated by an increase of the out-of-plane lattice parameter c. Hence the tetragonal distortion ratio c/a increases and may raise above $c/a = 1$ causing the MCA to become positive. Experimentally we observe a reduction rather than a vanishing of the in-plane spin asymmetry, which is compatible with a tilting of the magnetization towards the film normal rather than a complete reorientation to the out-of-plane configuration. Note, however, that the above consideration does not account for shape anisotropy or low-anisotropy domain configurations[12] that can lead to a distribution of moment orientations with a significant total in-plane component in spite of the positive MCA, which favors out-of-plane magnetization.

V. CONCLUSION

Epitaxial equiatomic FeRh thin films were deposited on MgO(001) and investigated by SEMPA and MOKE without intermediate exposure to ambient pressure. MOKE confirmed the presence of the AFM-to-FM metamagnetic phase transition in the body of the film between 143 K and RT. The surface domain images measured by the extremely surface-sensitive SEMPA revealed FM domains covering the whole surface at all temperatures between 122 and 450 K proving that the previously reported interfacial ferromagnetism[13,14] occurring even in the temperature range of the AFM phase in the body of the film is an intrinsic property of the unperturbed FeRh(001) surface rather than an artifact induced by capping layers. The analysis of the SEMPA images in terms of two-dimensional spin asymmetry histograms revealed a strong decrease of the in-plane magnetization upon cooling between 400 and 350 K that is attributed to a partial spin reorientation transition at the very surface. In contrast to previous reports,[10,12] the spin reorientation and metamagnetic transitions did not occur at the same temperature denying for the present case that the spin reorientation is induced by the volume expansion at the AFM-to-FM transition. Instead a model for a temperature-driven spin reorientation transition in the FM phase is proposed based on DFT calculations of the strain-induced

magneto-crystalline anisotropy of FeRh by Bordel *et al.*[12] and taking into account the different thermal expansion coefficients of MgO and FeRh. This study of uncapped and non-oxidized FeRh thin films has led to a better understanding of the intrinsic magnetic properties of this fascinating and potentially technologically relevant material.

ACKNOWLEDGMENT

This work was supported by the Chinese Scholarship Council under grant number 2009612002.

[1] A. I. Zakharov, A. M. Kadomtseva, R. Z. Levitin, and E. G. Ponyatovskii, Sov. Phys. JETP **19**, 1348 (1964).
[2] J.-U. Thiele, S. Maat, and E. E. Fullerton, Appl. Phys. Lett. **82**, 2859 (2003).
[3] J.-U. Thiele, S. Maat, J. Robertson, and E. Fullerton, IEEE Trans. Magn. **40**, 2537 (2004).
[4] X. Marti, I. Fina, C. Frontera, J. Liu, P. Wadley, Q. He, R. J. Paull, J. D. Clarkson, J. Kudrnovský, I. Turek, J. Kuneš, D. Yi, J.-H. Chu, C. T. Nelson, L. You, E. Arenholz, S. Salahuddin, J. Fontcuberta, T. Jungwirth, and R. Ramesh, Nat. Mat. **13**, 367 (2014).
[5] R. O. Cherifi, V. Ivanovskaya, L. C. Phillips, A. Zobelli, I. C. Infante, E. Jacquet, V. Garcia, S. Fusil, P. R. Briddon, N. Guiblin, A. Mougin, A. A. Ünal, F. Kronast6, S. Valencia, B. Dkhil, A. Barthélémy, and M. Bibes, Nat. Commun. **13**, 345 (2014).
[6] M. Fallot, Ann. Phys. **10**, 291 (1938).
[7] J. S. Kouvel and C. C. Hartelius, J. Appl. Phys. **33**, 1343 (1962).
[8] G. Shirane, C. W. Chen, P. A. Flinn, and R. Nathans, Phys. Rev. **131**, 183 (1963).
[9] S. Maat, J.-U. Thiele, and E. E. Fullerton, Phys. Rev. B **72**, 214432 (2005).
[10] J. Cao, N. T. Nam, S. Inoue, H. Y. Y. Ko, N. N. Phuoc, and T. Suzuki, J. Appl. Phys. **103**, 07F501 (2008).
[11] M. Sharma, H. M. Aarbogh, J.-U. Thiele, S. Maat, E. E. Fullerton, and C. Leighton, J. Appl. Phys. **109**, 083913 (2011).
[12] C. Bordel, J. Juraszek, D. W. Cooke, C. Baldasseroni, S. Mankovsky, J. Minár, H. Ebert, S. Moyerman, E. E. Fullerton, and F. Hellman, Phys. Rev. Lett. **109**, 117201 (2012).
[13] C. Baldasseroni, C. Bordel, A. X. Gray, A. M. Kaiser, F. Kronast, J. Herrero-Albillos, C. M. Schneider, C. S. Fadley, and F. Hellman, Appl. Phys. Lett. **100**, 262401 (2012).
[14] Y. Ding, D. A. Arena, J. Dvorak, M. Ali, C. J. Kinane, C. H. Marrows, B. J. Hickey, and L. H. Lewis, J. Appl. Phys. **103**, 07B515 (2008).
[15] J. W. Kim, P. J. Ryan, Y. Ding, L. H. Lewis, M. Ali, C. J. Kinane, B. J. Hickey, C. H. Marrows, and D. A. Arena, Appl. Phys. Lett. **95**, 222515 (2009).
[16] M. J. McLaren, M. A. de Vries, R. M. D. Brydson, and C. Marrows, J. Phys.: Conf. Ser. **371**, 012031 (2012).
[17] M. Loving, M. A. de Vries, F. Jimenez-Villacorta, C. Le Graet, X. Liu, R. Fan, S. Langridge, D. Heiman, C. H. Marrows, and L. H. Lewis, J. Appl. Phys. **112**, 043512 (2012).
[18] Y. Yokoyama, M. Usukura, S. Yuasa, Y. Suzuki, H. Miyajima, and T. Katayama, J. Magn. Magn. Mater. **177**, 181 (1998).
[19] M. Manekar, C. Mukherjee, and S. B. Roy, Europhys. Lett. **80**, 17004 (2007).
[20] Z. Q. Qiu and S. D. Bader, Rev. Sci. Inst. **71**, 1243 (2000).
[21] K. Koike and K. Hayakawa, Jpn. J. Appl. Phys. **23**, L187 (1984).
[22] J. Unguris, G. Hembree, R. J. Celotta, and D. T. Pierce, J. Microscopy **139**, RP1 (1985).
[23] H. P. Oepen and J. Kirschner, Phys. Rev. Lett. **62**, 819 (1989).
[24] R. Allenspach, M. Stampanoni, and A. Bischof, Phys. Rev. Lett. **65**, 3344 (1990).
[25] J. Unguris, R. J. Celotta, and D. T. Pierce, Phys. Rev. Lett. **69**, 1125 (1992).
[26] H. P. Oepen, G. Steierl, and J. Kirschner, J. Vac. Sci. Technol. B **20**, 2535 (2002).
[27] D. Yu, C. Math, M. Meier, M. Escher, G. Rangelov, and M. Donath, Surf. Sci. **601**, 5803 (2007).
[28] J. Kirschner and R. Feder, Phys. Rev. Lett. **42**, 1008 (1979).
[29] J. Kirschner, *Polarized Electrons at Surfaces* (Springer-Verlag, Berlin, 1985).
[30] R. Frömter, S. Hankemeier, H. P. Oepen, and J. Kirschner, Rev. Sci. Instr. **82**, 033704 (2011).
[31] FOCUS SPLEED Technical Reference Manual.
[32] M. Rickart, B. F. P. Roos, T. Mewes, J. Jorzick, S. O. Demokritov, and B. Hillebrands, Surf. Sci. **495**, 68 (2001).
[33] C. B. Alcock, V. P. Itkin, and M. K. Horrigan, Canadian Metallurgical Quarterly **23**, 309 (1984).
[34] J. M. Lommel, J. Appl. Phys. **37**, 1483 (1966).
[35] D. E. Bürgler, C. M. Schmidt, D. M. Schaller, F. Meisinger, R. Hofer, and H.-J. Güntherodt, Phys. Rev. B **56**, 4149 (1997).
[36] K. D. Childs, B. A. Carlson, L. A. LaVanier, J. F. Moulder, D. F. Paul, W. F. Stickle, and D. G. Watson, *Handbook of Auger Electron Spectroscopy*, 3rd ed. (Physical Electronics Inc, Minnesota, 1995).
[37] P. E. M. Hofer and P. E. Cucka, J. Phys. Chem. **27**, 1552 (1966).
[38] J. S. Kouvel, J. Appl. Phys. **37**, 1257 (1966).
[39] P. Tu, A. J. Heeger, J. S. Kouvel, and J. B. Comly, J. Appl. Phys. **40**, 1368 (1969).
[40] S. Inoue, H. Y. Y. Ko, and T. Suzuki, IEEE Trans. Magn. **44**, 2875 (2008).
[41] G. K. White and O. L. Anderson, J. Appl. Phys. **37**, 430 (1966).
[42] *II-VI and I-VII Compounds; Semimagnetic Compounds*, edited by O. Madelung, U. Rössler, and M. Schultz (Springer, Berlin Heidelberg, 1999), Chap. Magnesium oxide (MgO) crystal structure, lattice parameters, thermal expansion.
[43] M. R. Ibarra and P. A. Algarabel, Phys. Rev. B **50**, 4196 (1994).